

Laboratory friction and plastic flow laws predict transient deformation after subduction zone mega-quake

Ryoichiro Agata^{1*}, Sylvain D. Barbot², Kohei Fujita³, Mamoru Hyodo¹, Takeshi Iinuma¹, Ryoko Nakata¹, Tsuyoshi Ichimura³, Takane Hori¹

April 5, 2018

1. Japan Agency for Marine-Earth Science and Technology, Yokohama, Japan.
2. Earth Observatory of Singapore, Asian School of the Environment, Nanyang Technological University, Singapore.
3. Earthquake Research Institute, The University of Tokyo, Tokyo, Japan.

The deformation transient that follows large subduction zone earthquakes is thought to be the response of a large-scale nonlinear system where slip on the megathrust and viscoelastic flow in the asthenospheric mantle are accelerated by the sudden coseismic stress change[1]. However, as numerical models of such complex systems are still in their infancy, bringing together theory and prediction is still a major challenge. Here, we consider the post-earthquake deformation of the 2011 Mw 9.2 Tohoku-Oki earthquake based on numerical simulations incorporating a non-linear viscoelastic model[2, 3] and stress-driven afterslip[4, 5] in a fully three-dimensional (3D) heterogeneous structure of the subduction zone, using state-of-the-art techniques in computational science[6, 7]. The combination of power-law viscoelastic flow and afterslip results in good agreement in horizontal component of the calculated 2.8 year displacements with observation data[8, 9, 10, 11]: Viscoelastic flow associated with transient spatial variation of effective viscosity is dominant in overall deformation pattern with opposing horizontal direction on the seafloor and the land, while afterslip accounts for eastward displacement on land and offshore outside the rupture area. This suggests that post-earthquake deformation of large subduction zones earthquakes can be reasonably well anticipated when incorporating the frictional and rheological properties of lithosphere rocks derived from laboratory experiments into comprehensive models and a plausible structural model. Such three-dimensional, multi-physics simulations provide an effective framework to gain more detailed insight into the physical properties of subduction zones.

Post-earthquake deformation can be interpreted as a process of relaxing the stress perturbation caused by the earthquake rupture. It generally consists of the deformation due to continued, mostly aseismic slip on the megathrust (afterslip)[12] and viscoelastic relaxation in the asthenosphere [1]. Afterslip relaxes the stress perturbation by localized deformation in the region of the fault plane that surrounds the earthquake rupture. Viscoelastic flow relaxes the coseismic stress change by distributed, plastic deformation in the surrounding mantle [13, 14]. The post-earthquake deformation of the 2011 Mw 9.2 Tohoku-Oki earthquake was captured by a wide array of land-based[15, 8] and seafloor[9, 10, 11] instruments. This widespread observation network captured a complex post-earthquake deformation field. Some near-trench seafloor stations moved seaward, in the opposite direction to the long-term subduction motion, while others moved landward (Fig. 1a). The post-earthquake vertical motion was also complex, with many seafloor stations moving in opposing directions than that on land. Several studies [9, 10, 16, 17, 18] claim that viscoelastic relaxation largely contributed to these patterns.

33 The 2011 Mw 9.2 Tohoku-Oki earthquake induced a large stress perturbation in the surrounding
 34 lithosphere that accelerated the flow in the oceanic asthenosphere and in the mantle wedge. It is
 35 natural to expect that viscoelastic relaxation during the post-earthquake period can be described by
 36 the constitutive properties of peridotite, a rock assemblage of mostly pyroxene and olivine, under
 37 high temperature and pressure conditions. Likewise, afterslip may be described by the frictional
 38 properties of the megathrust. Laboratory experiments suggest that the plastic deformation of mantle
 39 rocks is accommodated by a thermally activated flow that obeys a power-law relation between stress
 40 and strain-rate [2, 3]. The friction between the subducting slab and the upper plate is governed
 41 by a laboratory-derived kinematic friction law [4, 5] that predicts the velocity of afterslip based on
 42 the stress evolution. Incorporating the laboratory-derived constitutive properties for plastic flow
 43 and afterslip successfully explained the deformation that followed the 2012 Mw 8.6 Indian Ocean
 44 earthquake [14], for which the surrounding rheological structure is rather simple. In contrast, most
 45 studies of the Tohoku-Oki earthquake employed simplified rheological models with linear viscoelastic
 46 flow in the mantle and kinematic afterslip [10, 19, 17] or explored more realistic rock properties in
 47 two-dimensional models [16, 20]. Despite recent efforts, simulating the full three-dimensional response
 48 of the Japan subduction zone still represents a significant challenge, probably due to the combination
 49 of the geometrical complexity and the nonlinear governing equations. Finite element techniques afford
 50 some of the most flexibility to build realistic simulations, but the remaining difficulty lies in the
 51 computational cost of such calculations.

52 Here, we exploit a state-of-the-art finite-element method proposed in computational science [6, 7]
 53 to simulate the three-dimensional response of the lithosphere-asthenosphere system following the 2011
 54 Mw 9.2 Tohoku-Oki earthquake with plastic flow in the mantle and afterslip on the megathrust. The
 55 approach also allows us to incorporate a realistic velocity structure for the Japanese margin, Earth’s
 56 sphericity and laboratory-derived, nonlinear rock constitutive properties. We assume that the plastic
 57 flow of the upper mantle is accommodated by steady-state dislocation creep, with the following stress-
 58 strain-rate relationship [2]

$$\dot{\epsilon} = K(C_{\text{OH}})^r \sigma^n \exp\left(\frac{H}{RT}\right) \quad (1)$$

59 where $\dot{\epsilon}$ is the norm of the strain-rate tensor, K is a pre-exponential factor, C_{OH} and r are the water
 60 concentration and its exponent, σ is the norm of deviatoric stress tensor, n is the stress exponent,
 61 $H = Q + p\Omega$ is the activation enthalpy, R is the universal gas constant, T is the temperature.
 62 The enthalpy incorporates the activation energy Q and the activation volume Ω and depends on the
 63 confining pressure p . As the model already exhibits significant complexity due to the coexistence of
 64 afterslip and viscoelastic flow with lateral variations of constitutive properties, and since its constitutive
 65 properties are still unclear, we ignore the transient creep that is thought to take place during the early
 66 stage of post-earthquake transients [21, 14]. We combine dislocation creep with diffusion creep, but the
 67 latter does not play a significant role in our short-term simulations (see Methods). The temperature
 68 profile is based on a two-dimensional model for the Tohoku region [22], which we expanded along strike
 69 with a mantle temperature of 1380°C (Fig. 1b), compatible with another study [14]. We converted the
 70 background shortening rate of 10^{-8} yr^{-1} to determine the background stress based on the rheological
 71 law [23]. We assume that the velocity of afterslip on the megathrust is governed by the rate- and
 72 state-dependent friction (see Methods for details), given by

$$V = V_* \exp\left(\frac{\tau - (\tau_{s*} + \Delta\tau_s)}{A}\right), \quad (2)$$

73 where τ is the shear traction, τ_{s*} is the steady-state frictional resistance, $\Delta\tau_s$ is a state variable [24]. A
 74 is a parameter that controls the fracture energy consumed during fault slip. For the initial condition
 75 of the simulation, we borrow the coseismic slip (Fig. 1a) and the fault constitutive properties (Fig. 1c
 76 and Extended Data Fig. 5b) from a simulation of giant earthquakes in the Tohoku region [25]. We
 77 divide the region into three plates: a continental plate that includes the North-American and Eurasian

78 plates and two oceanic plates, the Pacific and the Philippine Sea plates. Each tectonic plate consists
79 of an elastic layer near the surface (the crust and the lithospheric mantle) and a viscoelastic mantle
80 layer below (Fig. 1c and Fig. 2). The elastic and viscoelastic layers in the three plates share the same
81 elastic properties (Fig. 1c). Simulating the dynamics of this nonlinear system in three-dimensions with
82 realistic elastic, frictional, and plastic properties require a large-scale computation environment of 10^4
83 computer cores and a state-of-the-art fast and scalable finite element solver[6, 7] (see Methods).

84 Our simulated deformation shows similar patterns to the observation data for the cumulative 2.8
85 year post-earthquake displacement in the horizontal direction (Fig. 3a) when we choose the following
86 rock properties $K = 10^{0.56} \text{ MPa}^{-n}/\text{s}$, $C_{\text{OH}}=1,000 \text{ ppm H/Si}$, $Q=430 \text{ kJ/mol}$, $r=1.2$, $\Omega=13.5 \text{ cm}^3/\text{mol}$
87 and $n=3$ (see Methods). For simplicity, we assumed a similar average water content in the oceanic
88 asthenosphere and in mantle wedge, even though water concentration may be large in the mantle
89 wedge corner due to slab dehydration [26]. The values adopted for the activation energy and the
90 activation volume fall well within the uncertainties constrained by laboratory experiments [3], e.g., $Q =$
91 $410 \pm 50 \text{ kJ/mol}$ and $\Omega = 11 \pm 3 \text{ cm}^3/\text{mol}$, despite the required extrapolation to different temperature
92 and pressure conditions. This indicates that the physical and geological setting of the Japan subduction
93 zone is understood well enough to make accurate predictions about how the lithosphere-asthenosphere
94 system will deform in response to a large earthquake.

95 The temporal and spatial evolution of effective viscosity after the giant earthquake naturally results
96 from the nonlinear constitutive relation (1) and plays an important role in the rapid and complex
97 deformation that occurs during the post-earthquake period. In response to the large (above 1 MPa)
98 stress perturbation in the upper mantle, the effective viscosity (see Methods) was largely reduced
99 shortly after the earthquake in the depth of 80-180 km in the oceanic mantle and 100-200 km in the
100 mantle wedge (Fig. 4). The flow of low-viscosity mantle material below the trench axis drives westward
101 motion around the trench, explaining the continued displacement of the seafloor stations located above
102 the coseismic rupture (MYGI, KAMS and KAMN, Fig. 3b). The accelerated flow in the mantle wedge
103 contributes to the eastward displacement of GPS stations on land. Afterslip on the megathrust is
104 essential to explaining the deformation on land, but also the spatial pattern of displacement of the
105 seafloor stations, such as eastward displacement seen in the stations FUKU and MYGW (Fig. 3b).
106 Both these stations are in locations where viscoelastic flow produces little horizontal displacement,
107 making the post-earthquake response due to the afterslip dominant there (Fig. 4).

108 Despite the excellent fit at numerous stations in the far-field, there remain a few discrepancies
109 with the near-field data, presumably because our model does not include some details of the coseismic
110 rupture offshore. For example, the simulated horizontal displacement at the station FUKU is nearly
111 half of the measured one, despite a good agreement in the azimuthal direction. A peak of the amplitude
112 of afterslip in the green ellipse in Fig. 3b should be slightly closer to station FUKU to fit the data,
113 perhaps indicating that the coseismic slip was overestimated in this region. Such afterslip distribution
114 should also fit better the horizontal displacements in the southern part of the land area (the purple
115 ellipse in Fig. 3a). In the vertical displacement, significant uplift is observed in the fore-arc (The
116 purple circles in Fig. 4). In the trench-normal profile of the stations MYGI and MYGW, although
117 viscoelastic flow in the simulation produces uplift in this region, subsidence due to the afterslip cancels
118 it out (the green circles in Fig. 4). Furthermore, a significant portion of this uplift in viscoelastic flow
119 is due to stress change associated with afterslip, which we inferred from simulations of viscoelastic
120 flow that exclude afterslip (the green circles in Extended Data Fig. 8a). Without the interaction
121 between afterslip and viscoelastic flow, the computed 2.8-year horizontal displacements are reduced
122 by more than 10% in some of the land stations, and the vertical ones change by more than 30% in
123 many stations in both the land and the seafloor (Extended Data Fig. 8b). As afterslip in the near
124 field can be highly sensitive to the details of the coseismic rupture, these residuals may be caused by
125 still unresolved slip patterns of the mainshock. Despite these shortcomings, our results highlight the
126 nonlinear interactions among coseismic slip, afterslip and viscoelastic flow.

127 Remarkably, the spatial distribution of effective viscosity derived from laboratory data and co-
128 seismic stress change is similar to those inferred from optimization of simplified linear viscoelastic
129 models. The effective viscosity shortly after the earthquake is around $2 \times 10^{17} \text{ Pa s}$ at the minimum

130 both in mantle wedge and oceanic mantle. This is equivalent to the viscosity in a linear transient
 131 creep model that fits observed post-earthquake deformation during the early stage [10], which was
 132 attributed to the presence of fluid or partial melt in lithosphere-asthenosphere boundary (LAB) [10].
 133 Our result suggests that such a low-viscosity layer is the transient response of nonlinear plastic flow to
 134 the large stress perturbation, rather than a permanent structure. The linear viscoelastic models with
 135 low viscosity layers have only limited applicability in the context of a nonlinear viscoelastic model with
 136 both spatially and temporally varying effective viscosity (Extended Data Fig. 7). A recent experiment
 137 implied that a LAB is not explained by the presence of water[27], which supports our interpretation.

138 Our study demonstrates that a rheological model of the plate boundary based on independent
 139 geological and geophysical data can make realistic, first-order predictions of the transient response of
 140 the lithosphere following giant earthquakes. Complex post-earthquake deformation of a large subduc-
 141 tion zone earthquake can be well explained by taking into account the laboratory-derived friction and
 142 plastic flow laws in a three-dimensional structural model. The discrepancy between the simulation
 143 and the data should be reduced, in principle, by refined models of the coseismic rupture and the in
 144 situ conditions such as initial stress, temperature and confining pressure, properties that are usually
 145 constrained for long time scales [28, 29]. The approach is generally applicable to other ocean-continent
 146 subduction zones, implying that our understanding of rocks friction and plastic properties may be de-
 147 tailed enough to predict the slow deformation of the lithosphere during the interseismic period. The
 148 remaining challenge is to understand Earth’s deformation at high strain-rates.

149 Methods

150 0.1 Rheology model for upper mantle

151 We used the dislocation creep model based on the laboratory-derived power-law relation and the linear
 152 Maxwell element in series:

$$\dot{\varepsilon} = K(C_{\text{OH}})^r \sigma^n \exp\left(\frac{Q + p\Omega}{RT}\right) + \frac{1}{2\eta_l} \sigma, \quad (3)$$

153 where η_l is a constant value for viscosity in the linear Maxwell element. This simplifies the treatment of
 154 diffusion creep, based on the idea that viscosity in diffusion creep is 10^{1-2} times larger than effective
 155 viscosity in dislocation creep shortly after earthquakes of Mw 8.2 and 8.6[14], and the influence of
 156 diffusion creep is not expected to be very large in the 2.8 years deformation after the 2011 Mw 9.2
 157 Tohoku-Oki earthquake. We use $\eta_l = 1 \times 10^{19}$ Pa s for the whole of the region, which is nearly
 158 the average value of the viscosity structure estimated for steady state 2D model around the Japan
 159 Trench[23]. In tensor notation,

$$\dot{\varepsilon}_{ij} = K(C_{\text{OH}})^r |\sigma'_{ij}|^{n-1} \exp\left(\frac{Q + p\Omega}{RT}\right) \sigma'_{ij} + \frac{1}{2\eta_l} \sigma'_{ij}, \quad (4)$$

160 where the apostrophe denotes deviatoric tensor, and $|\cdot|$ is the norm of tensor (square root of the
 161 second invariant of the tensor). We defined effective viscosity to be $\eta_{\text{eff}} = \sigma/2\dot{\varepsilon}$, thus

$$\eta_{\text{eff}} = \frac{\eta_p \eta_l}{\eta_p + \eta_l} \quad (5)$$

162 where

$$\eta_p = \frac{1}{2K(C_{\text{OH}})^r} |\sigma'_{ij}|^{-n+1} \exp\left(-\frac{Q + p\Omega}{RT}\right). \quad (6)$$

163 Our temperature pattern (Fig. 1b) in the elastic slab is significantly different from the reference thermal
 164 model[22] in that it keeps a low temperature even in the depth deeper than 200 km. However, it affects
 165 little the simulation results because high pressure is dominant and does not allow much viscoelastic
 166 flow in this depth. In the simulation, we use the values proposed from laboratory experiments[3] for

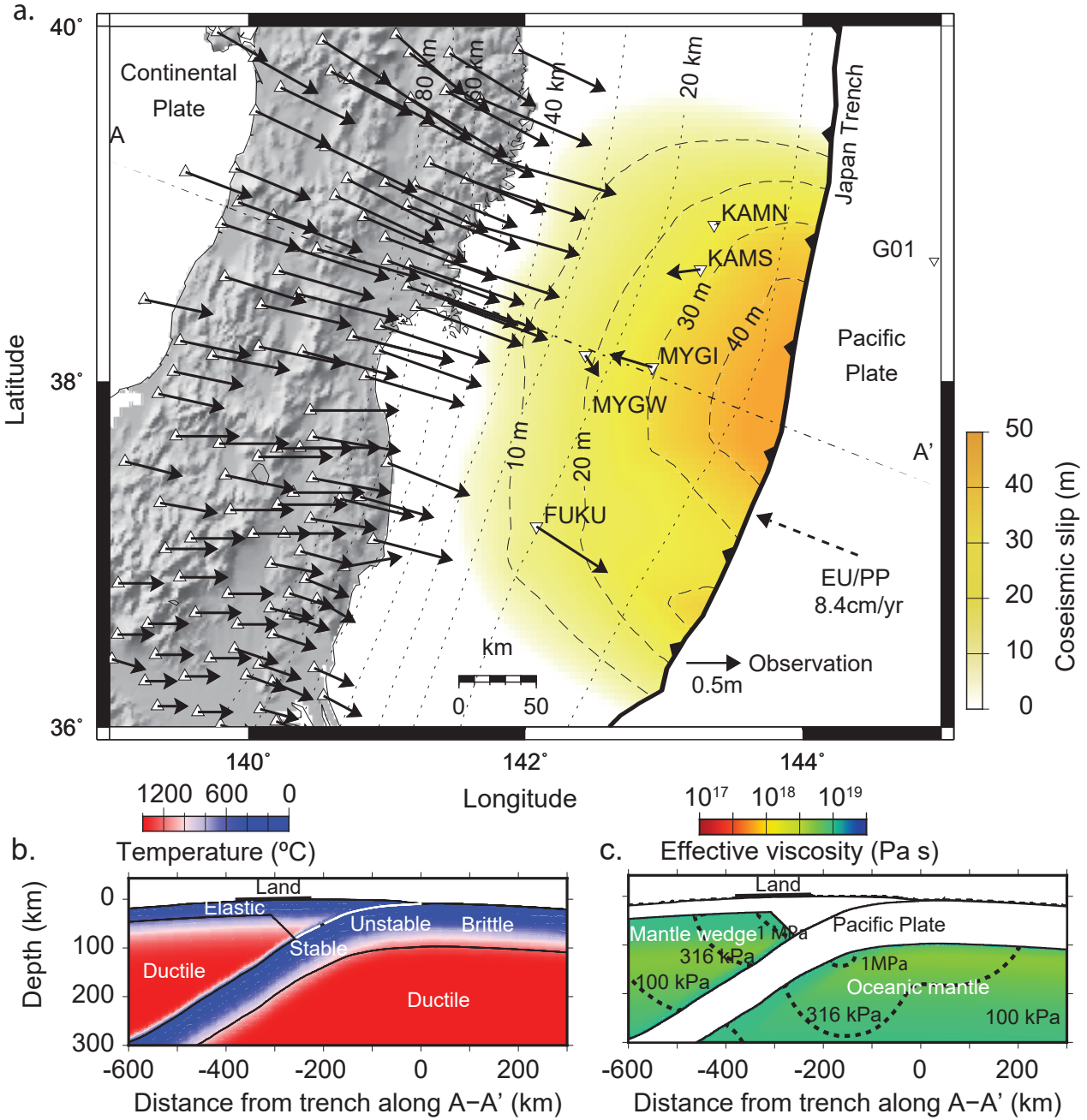


Figure 1: Post-earthquake deformation 2.8 years after the 2011 Tohoku-Oki Earthquake and surrounding material properties. a, Measured displacement in the land stations [15, 8] (triangles) and the seafloor stations [9, 11] (inverse triangles). We removed some land stations for visibility. Coseismic displacement is not available in the station G01. Dashed-dotted and dotted lines are the location of the cutting plane (A-A' profile) and the depth of the plate boundary, respectively. b, Assumed temperature structure and frictional properties in the A-A' profile. In the “unstable” region, where coseismic slip is input in our simulation, friction parameters are set as $-0.2 \text{ MPa} \leq A - B \leq -0.1 \text{ MPa}$ and $0.2 \text{ m} \leq L \leq 0.3 \text{ m}$. In the “stable” region, where afterslip occurs in our simulation, $A - B = 0.1 \text{ MPa}$ and $L = 13 \text{ m}$ (also see Extended Data Fig. 5b). The temperature values in the layers of elastic materials are not used in the simulation. c, The assumed viscoelastic structure and the stress change along the A-A' profile. The mantle wedge and oceanic mantle are viscoelastic with $\mu_v = 65 \text{ GPa}$. The remaining volume is elastic with $\mu_e = 45 \text{ GPa}$. Poisson's ratio is $\nu = 0.25$ and density is $\rho = 3300 \text{ kg m}^{-3}$ everywhere. The color indicates the effective viscosity before the earthquake and the computed stress distribution. Contribution from dislocation creep is dominant in the area with the light yellow, while viscosity in the linear term is dominant (see Methods) elsewhere. The dashed contour line indicates summation of background stress and coseismic stress (norm of deviatoric stress tensor).

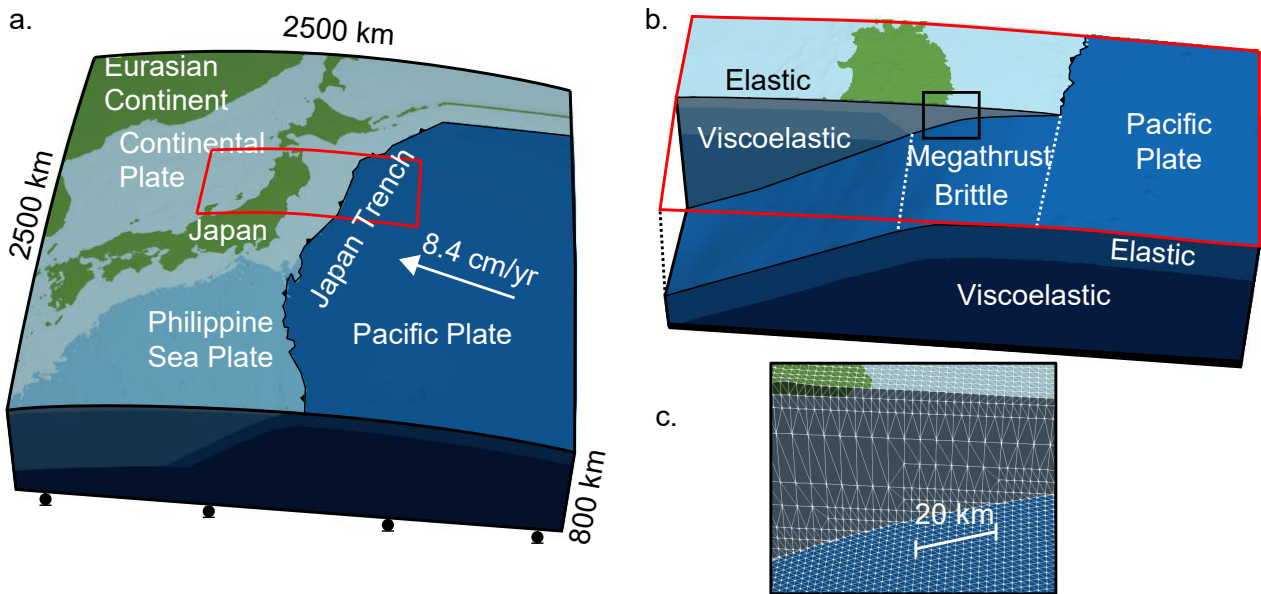


Figure 2: The finite-element model used in our study. **a.** Overview, **b.** close-up view for the region of the red rectangular in **a** with the location of the megathrust and **c.** close-up view for the region of the yellow rectangular in **b** with finite-element mesh patterns. The elements with the same color are in the same structural component (we have six of them, elastic and viscoelastic layer in three plates). The green color is used to distinguish the elements that are located above the sea level. The green elements have the same material properties as those in the continental plate.

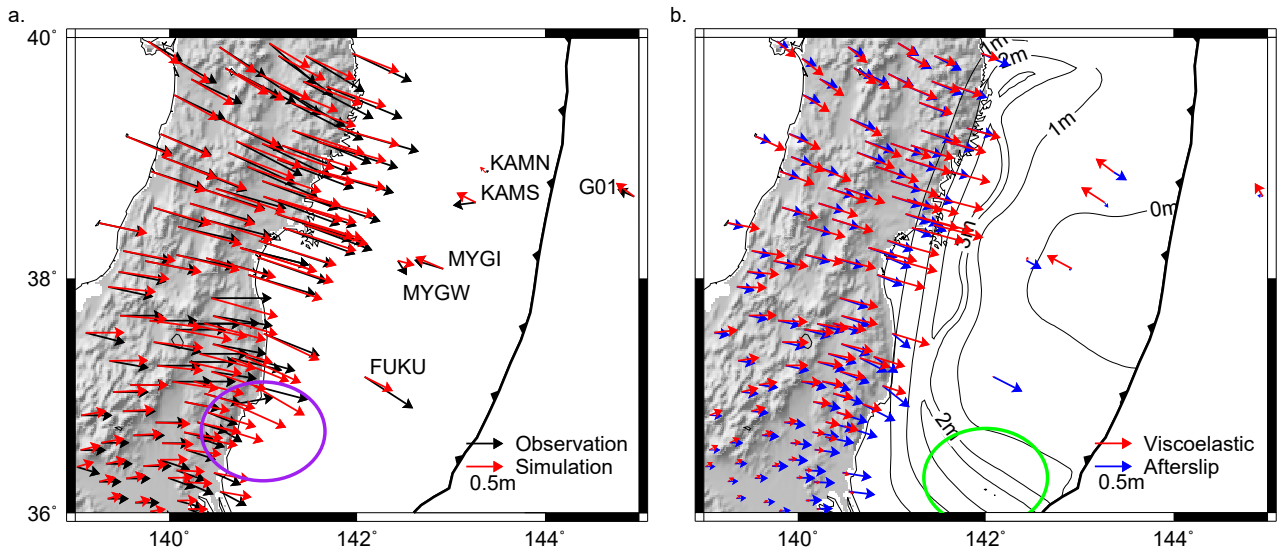


Figure 3: Post-earthquake deformation of the 2011 Tohoku-Oki earthquake. a, The horizontal component of 2.8-year post-earthquake displacements. In the station G01, displacement in the period 1.5 years and 2.8 years after the earthquake is plotted because of the limitation of data availability. In addition, the contribution from the plate convergence rate (shown in Fig. 1a), which is not included in our simulation scheme, is added to the simulation result in the station. b, The horizontal components of 2.8-year post-earthquake displacements in the simulation broken down into the contribution from afterslip and viscoelastic flow. The viscoelastic component includes the contribution from both coseismic slip and afterslip. The contour lines indicate accumulated afterslip for 2.8 years. A peak of the amplitude of afterslip in the green ellipse should be slightly closer to the station FUKU to fit better the horizontal displacements in FUKU and the purple ellipse.

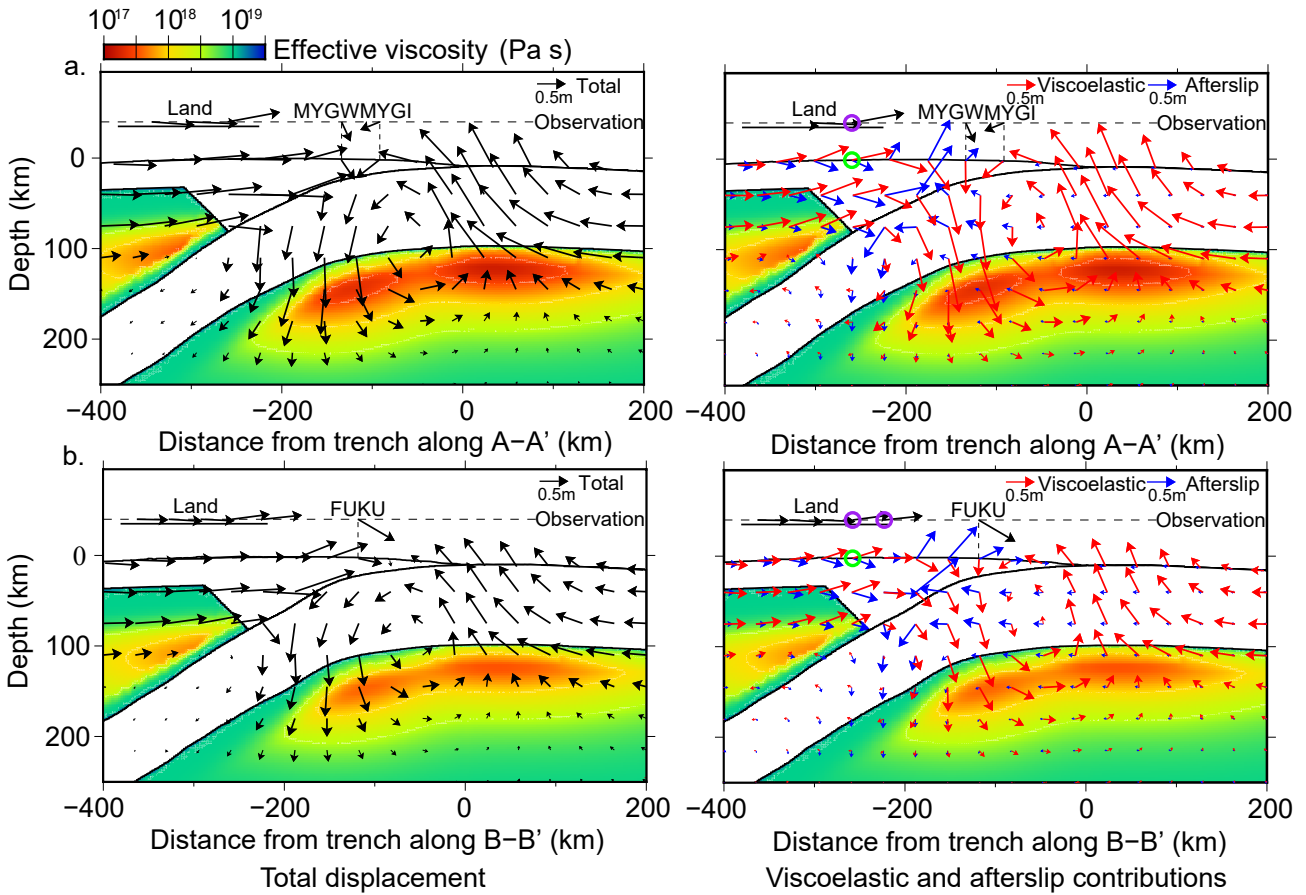


Figure 4: Simulation results on the cutting planes that are parallel to plate convergence direction, going through seafloor stations (a: the A-A' profile with MYGW and MYGI, b: the B-B' profile, which is parallel to A-A' and runs by the station FUKU). The figures on the left are for the total displacement after 2.8 years. The panels on the right show the contribution from afterslip and viscoelastic flow after 2.8 years. The color indicates the distribution of effective viscosity due to coseismic stress change. The black arrows on the horizontal dashed line are the observed displacements. In the location of purple circles, observation data shows uplift, while in the green circles, computed uplift viscoelastic displacement is canceled out by subsidence due to afterslip.

167 K , r and n , while Q and Ω were chosen within the error bar obtained in the same experiments, so
 168 that the computed displacement values are more consistent with the data. We set the C_{OH} value as
 169 an average in the upper mantle. Further study on more detailed variation of measured displacement
 170 should require considering heterogeneous distribution of water content[14, 30].

171 0.2 Coseismic slip and fault friction setting

172 To compute post-earthquake deformation, we take over an M9-class earthquake scenario calculated in
 173 an earthquake cycle simulation in the Tohoku region carried out by Nakata *et al.*[25]. This simulation
 174 supposes that space-time variations in slip velocity are assumed to be a slip with a frictional interface.
 175 We assume that equilibrium equation in shear stress on the fault plane, which is described as,

$$\frac{d\tau_i}{dt} = F_i(\mathbf{V} - \mathbf{V}_{pl}, \dot{\boldsymbol{\epsilon}}^{\text{inelastic}}) - \gamma \frac{dV_i}{dt} \quad (7)$$

176 where τ_i and V_i are shear stress and slip velocity on a FEM node i on the fault. V_i is in the direction
 177 opposite to the convergence rate (Fig. 1). \mathbf{V} and \mathbf{V}_{pl} are vectors whose components are V_i and V_{pli} ,
 178 the plate convergence rate. $V_{pl} = 8.4\text{cm/yr}$ is used for the whole region in this study. $\boldsymbol{\epsilon}^{\text{inelastic}}$
 179 is inelastic strain in the targeted 3D body. The second term introduces the effect of the seismic
 180 radiation damping[31]. We use $\gamma = 0.3\mu/2c$, which is used in Nakata *et al.*[25] to reproduce a shorter
 181 duration during the 2011 Tohoku-Oki earthquake[32], where μ is the rigidity and c is the shear wave
 182 velocity. In many studies the simulations with elastic homogeneous half-space have been carried out,
 183 where $\dot{\boldsymbol{\epsilon}}^{\text{inelastic}} = 0$. This makes F_i a linear function of \mathbf{V} and enable F_i to be discretized by the
 184 boundary integral equation method (BIEM). In this study, we evaluate F_i directly by using the finite
 185 element method (see Section 0.3), in which F_i can be a function of both \mathbf{V} and $\dot{\boldsymbol{\epsilon}}^{\text{inelastic}}$, and arbitrary
 186 geometry and material heterogeneity can be considered. It should be noted that a BIEM approach
 187 that can incorporate inelastic strain in elastic homogeneous half-space was proposed recently[33]. The
 188 rate- and state-dependent friction law is used to model frictional behavior on the plate interface as

$$V_i = V_* \exp\left(\frac{\tau_i - (\tau_{s*i} + \Delta\tau_{si})}{A_i}\right), \quad (8)$$

$$\frac{d\Delta\tau_{si}}{dt} = \frac{B_i}{L_i/V_*} \exp\left(-\frac{\Delta\tau_{si}}{B_i}\right) - \frac{B_i V_i}{L_i}. \quad (9)$$

189 (8) represents a fault constitutive law that determines V_i for a given τ_i and a value of $\tau_{si}(=\tau_{s*i} + \Delta\tau_{si})$,
 190 where $\Delta\tau_{si}$ is a state variable which is analogous to the ‘‘strength as a threshold’’ [24] and τ_{s*i} the steady
 191 state strength with $V_i = V_{pl}$. (9) is an aging law[5]. The frictional parameter B controls strength
 192 recovery, while L controls slip weakening. Time integration is performed using an adaptive time step
 193 fifth-order Runge-Kutta algorithm[34]. In our simulation, initial value of τ_i and $\Delta\tau_{si}$ is extracted from
 194 a time step right after the earthquake in the simulation of Nakata *et al.*[25](Extended Data Fig. 5a).
 195 The values are multiplied by 0.7, because the coseismic slip computed in their simulation fits best
 196 the coseismic crustal deformation data when multiplied by 0.7 (mentioned in the next paragraph).
 197 The initial value of V_i is calculated with (8). Frictional parameters are also the same as in Nakata *et al.*
 198 *et al.*[25], excluding that small patches for M7 earthquakes are removed (Extended data Fig. 5b).

199 Extended Data Fig. 6 shows the coseismic slip, the same as in Fig. 1, which we extracted from
 200 the cycle simulation results, and comparison between computed and observed coseismic displacement.
 201 Although this slip model is not inferred from observation data, it fits the horizontal component of
 202 coseismic crustal deformation data well when multiplied by 0.7. The stress distribution computed in
 203 response to this coseismic slip is used as the stress perturbation to compute power-law viscoelastic
 204 flow and afterslip evolution.

205 0.3 Finite-element modeling

206 In the finite-element modeling, we discretize the equations for viscoelastic deformation and fault
 207 friction using the mesh shown in Fig. 2. The mesh was constructed using an updated version of

208 a meshing technique for quadratic tetrahedral elements based on a background structured grid[7].
 209 In the method, at first a uniform background cell covering entire targeted domain was used, and it
 210 defined the resolution of the layer interfaces as ds . The geometries of the ground surface and interfaces
 211 were simplified slightly to maintain good element quality. At the same time, unnecessary elements
 212 were merged to generate larger elements elsewhere. This method enables automated and robust
 213 construction of high-resolution tetrahedral mesh directly from digital elevation model (DEM) data
 214 of crustal structure without creating a CAD (computer-aided design) model. The updated version
 215 of the meshing algorithm carries out an additional post process to minimize the simplification of the
 216 geometry in the ground surface and interfaces as much as possible. Input elevation data sets are
 217 based on 900 m resolution topography data (JTOPO30), the CAMP model[35] and a velocity data
 218 set for the Japanese Island[36]. With $ds = 2$ km and little simplification of the geometry, shear stress
 219 distribution on the fault, which is essential for computing stress-driven afterslip, is evaluated accurately
 220 in the target problem. The finite element mesh has 1,402,810,116 degree-of-freedom (DOF) and
 221 346,885,129 tetrahedral elements. In viscoelastic material and elastic material, rigidity is $\mu_v = 65$ GPa
 222 and $\mu_e = 45$ GPa, respectively. Poisson's ratio is $\nu = 0.25$ and density is $\rho = 3300$ kg m⁻³ everywhere.
 223 This setting follows Sun et al. (2014)[10].

224 To evaluate F_i in (7), we applied an algorithm based on a viscoelastic finite element formulation[37,
 225 38], which we modified to consider nonlinear viscoelasticity. Slip velocity \mathbf{V} is input to the finite-
 226 element model using the split node technique[39] to evaluate response displacement rate. We con-
 227 sider the effect of gravity using surface gravity approximation[40]. Since no inertia term is in-
 228 cluded in the equations, the problem is quasi-static, which ends up with solving an elliptic problem
 229 in every time step. It means we need to solve the system which has billions of DOF. We intro-
 230 duced a modified version[41] of a massively-parallel FEM solver for computing crustal deformation[7]
 231 based on "GAMERA"[6] (a physics-based seismic wave amplification simulator, enhanced by a multi-
 232 Grid method, Adaptive conjugate gradient method, Mixed precision arithmetic, Element-by-element
 233 method, and pRedictor by Adams-Bashforth method).

234 We run the calculation using 2048 computer nodes (16384 computer cores) of the K computer
 235 at RIKEN, Advanced Institute for Computational Science[42], each computer node of which has one
 236 CPU (Fujitsu SPARC64 VIIIfx 8 core 2.0 GHz) and 16 GB of memory, for 7.5 hours to obtain the
 237 post-earthquake deformation for 2.8 years shown in Fig 3.

238 0.4 Viscoelastic and afterslip contributions

239 Fig. 3b and the figures in the right in Fig. 4 present breakdown of computed displacement into contri-
 240 bution from viscoelastic flow and afterslip. This is calculated in the following manner:

- 241 1. Extract accumulated 2.8 year afterslip distribution that is computed based on the nonlinear
 242 interaction of the rate- and state-dependent friction law and the nonlinear rock constitutive
 243 properties in the original simulation.
- 244 2. Compute elastic response displacement $\mathbf{u}_{\text{afterslip}}$ due to the extracted afterslip. $\mathbf{u}_{\text{afterslip}}$ corre-
 245 sponds to the blue arrows in Fig. 3 and 4.
- 246 3. $\mathbf{u}_{\text{viscoelastic}} = \mathbf{u}_{\text{original}} - \mathbf{u}_{\text{afterslip}}$, where $\mathbf{u}_{\text{viscosity}}$ and $\mathbf{u}_{\text{original}}$ correspond to the red and black
 247 arrows in Fig. 3 and 4, respectively.

248 We also present a result post-earthquake deformation simulation with "no interaction" between
 249 viscoelastic flow and afterslip (Extended Data Fig 8). In this simulation, we computed viscoelastic
 250 flow without the friction law (the red arrows in Extended Data Fig 8a), while computing afterslip
 251 without the nonlinear rock constitutive properties, only with pure elasticity. We finally summed up
 252 these to compute total deformation without their interaction (the red arrows in Extended Data Fig
 253 8b).

254 **Acknowledgement** This study was partially supported by JSPS Fellowship (26-8867). We obtained
 255 the results using the K computer at the RIKEN Advanced Institute for Computational Science

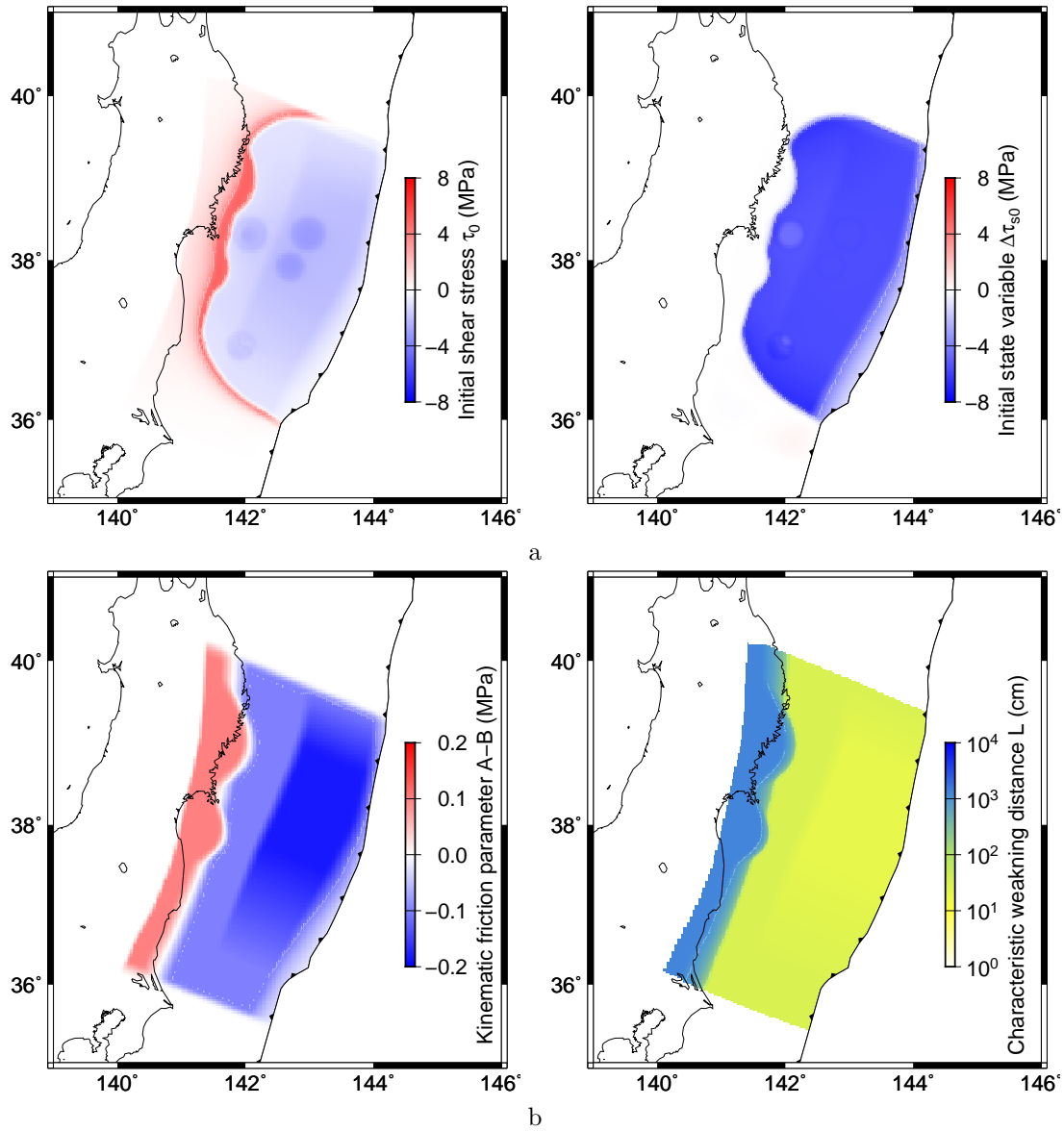


Figure 5: (Extended Data) The variables and parameters taken over from Nakata et al.[25]. a, Shear stress and state variable. Initial value of slip velocity V_i is calculated using these values with (8). b, Frictional parameters.

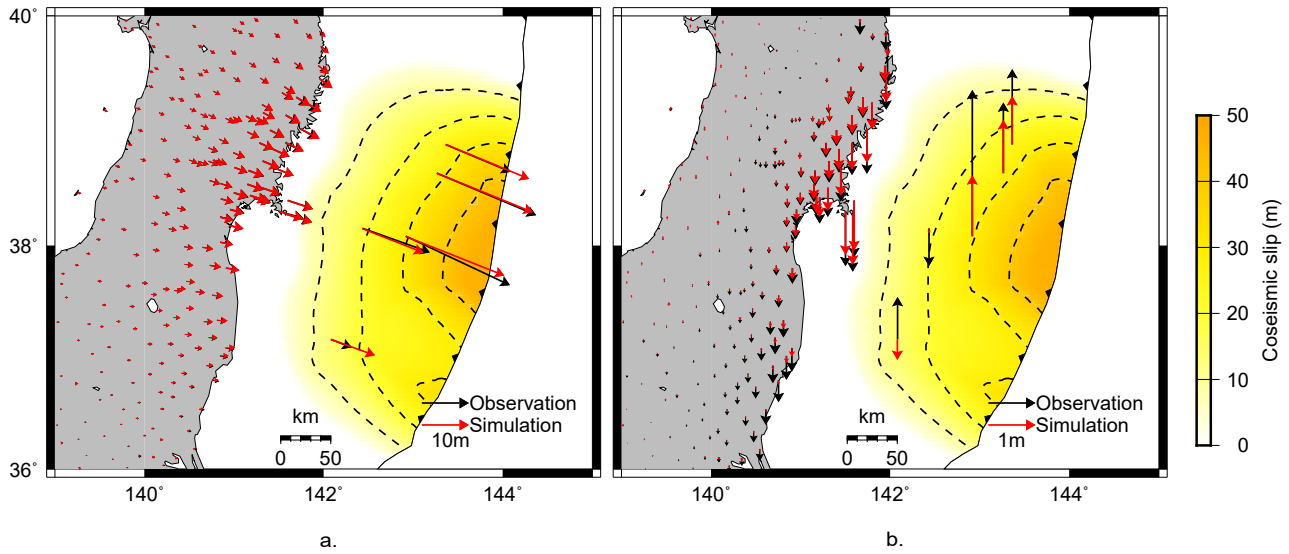


Figure 6: (Extended Data) Input coseismic slip based on Nakata *et al.*[25] and comparison between computed and observed coseismic displacement, including both the land[15, 43] and seafloor stations[44].

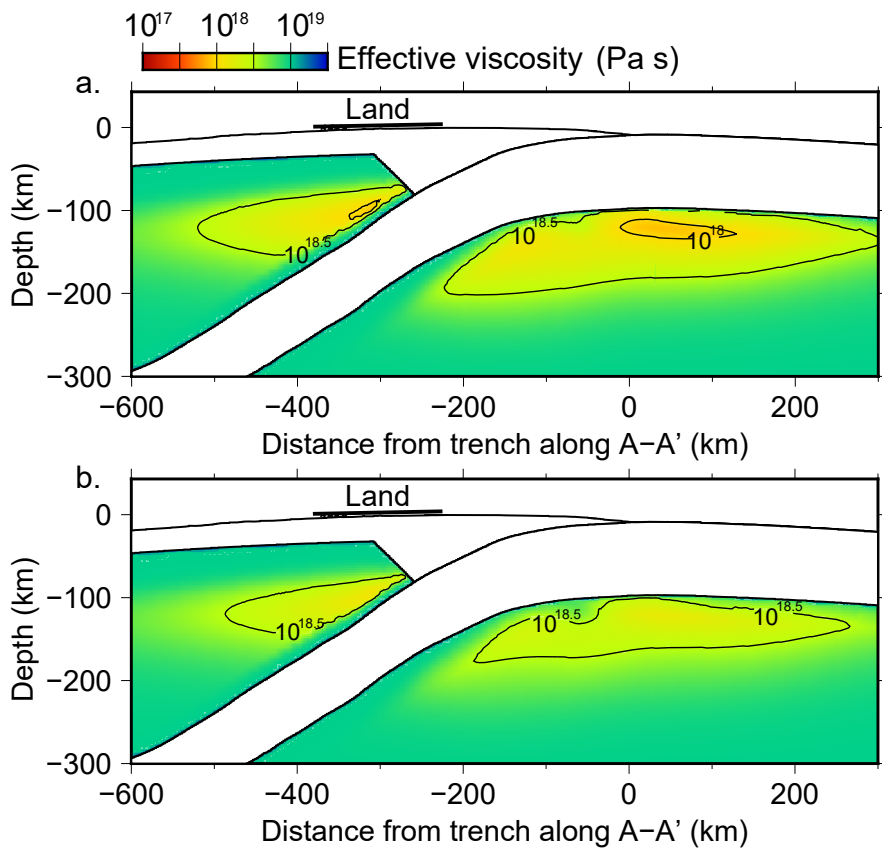


Figure 7: (Extended Data) Distributions of effective viscosity at a, 1 year and b, 2.8 years after the earthquake. The distribution of viscosity varies with time.

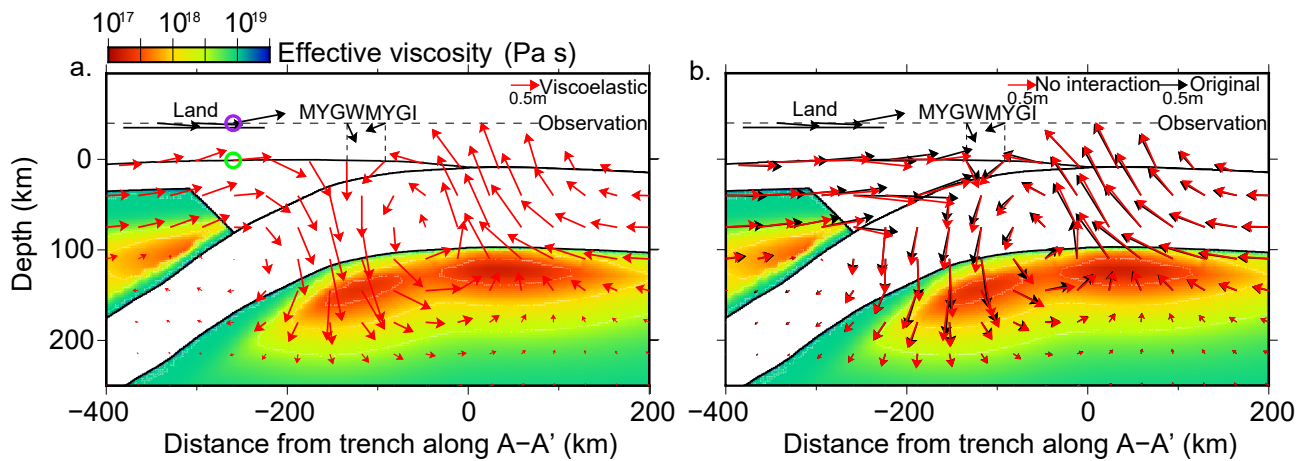


Figure 8: (Extended Data) a, Power-law viscoelastic flow in 2.8 years without considering afterslip in the cutting plane of the station MYGI and MYGW. In the green circle, uplift is significantly smaller than in the case with afterslip, shown in Fig. 4a. b, Comparison between the total 2.8-year displacement in the original simulation (black, the same as "total" in Fig. 4) and the result without interaction between afterslip and viscoelastic flow (red). As a result, the computed horizontal displacements are reduced by more than 10% in some of the land stations, and the vertical ones change by more than 30% in many stations in both of the land and the seafloor.

256 (Proposal number hp160221 and hp170249). This work was supported by Post K computer
 257 project (Priority issue 3: Development of Integrated Simulation Systems for Hazard and Disaster
 258 Induced by Earthquake and Tsunami).

259 **Author Contributions** R.A. and T.H. designed and conducted the study. R.A, S.D.B. and T.H.
 260 wrote the manuscript. R.A., K.F. and T. Ichimura wrote the simulation code. S.D.B. and
 261 M.H. contributed to refining the simulation algorithm. S.D.B. and T. Iinuma contributed to the
 262 modeling. R.N. prepared data for afterslip calculation.

263 **Materials & Correspondence** Correspondence and requests for materials should be addressed to
 264 R.A. (email: agatar@jamstec.go.jp).

265 References

- 266 [1] Wang, K., Hu, Y. & He, J. Deformation cycles of subduction earthquakes in a viscoelastic Earth.
 267 *Nature* **484**, 327–32 (2012). URL <http://www.ncbi.nlm.nih.gov/pubmed/22517160>.
- 268 [2] Hirth, G. & Kohlstedt, D. Rheology of the upper mantle and the mantle wedge: A view from the
 269 experimentalists. *Inside the subduction Factory* 83–105 (2003).
- 270 [3] Karato, S. & Jung, H. Effects of pressure on high-temperature dislocation creep in olivine.
 271 *Philosophical Magazine* **83**, 401–414 (2003).
- 272 [4] Dieterich, J. H. Modeling of rock friction: 1. experimental results and constitutive equations.
 273 *Journal of Geophysical Research: Solid Earth* **84**, 2161–2168 (1979).
- 274 [5] Ruina, A. Slip instability and state variable friction laws. *Journal of Geophysical Research: Solid*
 275 *Earth* **88**, 10359–10370 (1983).
- 276 [6] Ichimura, T. *et al.* Physics-based urban earthquake simulation enhanced by 10^7 BlnDOF \times 30
 277 K time-step unstructured FE non-linear seismic wave simulation. *SC14: International Conference*
 278 *for High Performance Computing, Networking, Storage and Analysis* 15–26 (2014).

- 279 [7] Ichimura, T. *et al.* An elastic/viscoelastic finite element analysis method for crustal deformation
280 using a 3-d island-scale high-fidelity model. *Geophysical Journal International* **206**, 114–129
281 (2016).
- 282 [8] Ozawa, S. *et al.* Coseismic and postseismic slip of the 2011 magnitude-9 Tohoku-Oki earthquake.
283 *Nature* **475**, 373–376 (2011). URL <http://www.ncbi.nlm.nih.gov/pubmed/21677648>.
- 284 [9] Watanabe, S. *et al.* Evidence of viscoelastic deformation following the 2011 Tohoku-oki earthquake
285 revealed from seafloor geodetic observation. *Geophysical Research Letters* (2014). URL <http://doi.wiley.com/10.1002/2014GL061134>.
286
- 287 [10] Sun, T. *et al.* Prevalence of viscoelastic relaxation after the 2011 Tohoku-oki earthquake. *Nature*
288 **514**, 84–87 (2014). URL <http://www.nature.com/doi/10.1038/nature13778>.
- 289 [11] Tomita, F. *et al.* First measurement of the displacement rate of the pacific plate near the japan
290 trench after the 2011 tohoku-oki earthquake using gps/acoustic technique. *Geophysical Research*
291 *Letters* **42**, 8391–8397 (2015).
- 292 [12] Hsu, Y.-J. *et al.* Frictional afterslip following the 2005 nias-simeulue earthquake, sumatra. *Science*
293 **312**, 1921–1926 (2006).
- 294 [13] Freed, A. M. & Bürgmann, R. Evidence of power-law flow in the mojave desert mantle. *Nature*
295 **430**, 548–551 (2004).
- 296 [14] Masuti, S., Barbot, S. D., Karato, S., Feng, L. & Banerjee, P. Upper-mantle water stratification
297 inferred from observations of the 2012 indian ocean earthquake. *Nature* **538**, 373–377 (2016).
- 298 [15] Miyazaki, S. & Y., H. The outlines of the geonet in japanese. *Meteorol. Res. Note* **192**, 105–131
299 (1998).
- 300 [16] Muto, J. *et al.* Heterogeneous rheology controlled postseismic deformation of the 2011 Tohoku-Oki
301 earthquake. *Geophysical Research Letters* **43**, 4971–4978 (2016).
- 302 [17] Freed, A. M. *et al.* Resolving depth-dependent subduction zone viscosity and afterslip from
303 postseismic displacements following the 2011 tohoku-oki, japan earthquake. *Earth and Planetary*
304 *Science Letters* **459**, 279–290 (2017).
- 305 [18] Noda, A., Takahama, T., Kawasato, T. & Matsu?ura, M. Interpretation of offshore crustal
306 movements following the 2011 tohoku-oki earthquake by the combined effect of afterslip and
307 viscoelastic stress relaxation. *Pure and Applied Geophysics* **175**, 559–572 (2018).
- 308 [19] Suito, H. Importance of rheological heterogeneity for interpreting viscoelastic relaxation caused
309 by the 2011 tohoku-oki earthquake. *Earth, Planets and Space* **69**, 21 (2017).
- 310 [20] Sobolev, S. V. & Muldashev, I. A. Modeling Seismic Cycles of Great Megathrust Earthquakes
311 Across the Scales With Focus at Postseismic Phase. *Geochemistry, Geophysics, Geosystems* **18**
312 (2017). URL <http://doi.wiley.com/10.1002/2017GC007230>.
- 313 [21] Freed, A. M., Herring, T. & Bürgmann, R. Steady-state laboratory flow laws alone fail to explain
314 postseismic observations. *Earth and Planetary Science Letters* **300**, 1–10 (2010).
- 315 [22] Syracuse, E. M., van Keken, P. E. & Abers, G. A. The global range of subduction zone thermal
316 models. *Physics of the Earth and Planetary Interiors* **183**, 73–90 (2010).
- 317 [23] Muto, J. *et al.* Two-dimensional viscosity structure of the northeastern Japan islands arc-trench
318 system. *Geophysical Research Letters* **40**, 4604–4608 (2013). URL <http://doi.wiley.com/10.1002/grl.50906>.
319

- 320 [24] Nakatani, M. Conceptual and physical clarification of rate and state friction: Frictional sliding
321 as a thermally activated rheology **106** (2001).
- 322 [25] Nakata, R., Hori, T., Hyodo, M. & Ariyoshi, K. Possible scenarios for occurrence of $m \sim 7$
323 interplate earthquakes prior to and following the 2011 tohoku-oki earthquake based on numerical
324 simulation. *Scientific reports* **6** (2016).
- 325 [26] Ji, Y., Yoshioka, S. & Matsumoto, T. *Journal of Geophysical Research : Solid Earth* 4458–4482
326 (2016).
- 327 [27] Cline II, C. J., Faul, U. H., David, E. C., Berry, A. J. & Jackson, I. Redox-influenced seismic
328 properties of upper-mantle olivine. *Nature* **555**, 355 (2018). URL [http://dx.doi.org/10.1038/](http://dx.doi.org/10.1038/nature25764)
329 [nature25764](http://dx.doi.org/10.1038/nature25764){\%}0Ahttp://10.0.4.14/nature25764.
- 330 [28] Van Keken, P. E., Kiefer, B. & Peacock, S. M. High-resolution models of subduction zones:
331 Implications for mineral dehydration reactions and the transport of water into the deep mantle.
332 *Geochemistry, Geophysics, Geosystems* **3** (2002).
- 333 [29] Morishige, M. & van Keken, P. E. Along-arc variation in the 3-d thermal structure around the
334 junction between the japan and kurile arcs. *Geochemistry, Geophysics, Geosystems* **15**, 2225–2240
335 (2014).
- 336 [30] Horiuchi, S. S. & Iwamori, H. A consistent model for fluid distribution, viscosity distribution,
337 and flow-thermal structure in subduction zone. *Journal of Geophysical Research: Solid Earth*
338 **121**, 3238–3260 (2016).
- 339 [31] Rice, J. R. Spatio-temporal complexity of slip on a fault. *Journal of Geophysical Research: Solid*
340 *Earth* **98**, 9885–9907 (1993).
- 341 [32] Thomas, M. Y., Lapusta, N., Noda, H. & Avouac, J.-P. Quasi-dynamic versus fully dynamic
342 simulations of earthquakes and aseismic slip with and without enhanced coseismic weakening.
343 *Journal of Geophysical Research: Solid Earth* **119**, 1986–2004 (2014).
- 344 [33] Lambert, V. & Barbot, S. Contribution of viscoelastic flow in earthquake cycles within the
345 lithosphere-asthenosphere system. *Geophysical Research Letters* **43**, 10,142–10,154 (2016).
- 346 [34] Press, W. H., Teukolsky, S. A., Vetterling, W. T. & Flannery, B. P. *Numerical Recipes in C*
347 *(2Nd Ed.): The Art of Scientific Computing* (Cambridge University Press, New York, NY, USA,
348 1992).
- 349 [35] Hashimoto, C., Fukui, K. & Matsu'ura, M. 3-D Modelling of Plate Interfaces and Numerical
350 Simulation of Long-term Crustal Deformation in and around Japan. *Pure and Applied Geophysics*
351 **161**, 2053–2068 (2004). URL <http://link.springer.com/10.1007/s00024-004-2548-8>.
- 352 [36] Koketsu, K., Miyake, H., Fujiwara, H. & Hashimoto, T. Progress towards a japan integrated
353 velocity structure model and long-period ground motion hazard map. *Proceedings of the 14th*
354 *World conference on earthquake engineering* S10–038 (2008).
- 355 [37] Parker, J. *et al.* Geophysical Finite-Element Simulation Tool (GeoFEST): Algorithms and Val-
356 idation for Quasistatic Regional Faulted Crust Problems. *Pure and Applied Geophysics* **165**,
357 497–521 (2008). URL <http://link.springer.com/10.1007/s00024-008-0325-9>.
- 358 [38] Hughes, J. R. & Taylor, R. L. Unconditionally stable algorithms for quasi-static elastovisco-
359 plastic finite element analysis. *Computers & Structures* **8**, 169–173 (1978).
- 360 [39] Melosh, H. & Raefsky, A. A simple and efficient method for introducing faults into finite element
361 computations. *Bulletin of the Seismological Society of America* **71**, 1391–1400 (1981). URL
362 <http://www.bssaonline.org/content/71/5/1391.short>.

- 363 [40] Segall, P. *Earthquake and volcano deformation* (Princeton University Press, 2010).
- 364 [41] Agata, R. *et al.* An adjoint-based simultaneous estimation method of the asthenosphere's vis-
365 cosity and afterslip using a fast and scalable finite element adjoint solver. *Geophysical Journal*
366 *International*, in press (2017).
- 367 [42] Miyazaki, H. *et al.* Overview of the k computer system. *Fujitsu Scientific and Technical Journal*
368 **48**, 255–265 (2012).
- 369 [43] Ohzono, M. *et al.* Strain anomalies induced by the 2011 tohoku earthquake (m w 9.0) as observed
370 by a dense gps network in northeastern japan. *Earth, planets and space* **64**, 17 (2012).
- 371 [44] Sato, M. *et al.* Displacement above the hypocenter of the 2011 Tohoku-Oki earthquake. *Science*
372 *(New York, N.Y.)* **332**, 1395 (2011). URL <http://www.ncbi.nlm.nih.gov/pubmed/21596950>.